



Pergamon

Acta mater. 49 (2001) 1677–1686



www.elsevier.com/locate/actamat

THE EFFECT OF CELL WALL MICROSTRUCTURE ON THE DEFORMATION AND FRACTURE OF ALUMINIUM-BASED FOAMS

A. E. MARKAKI and T. W. CLYNE[†]

Department of Materials Science and Metallurgy, Cambridge University, Pembroke Street, Cambridge CB2 3QZ, UK

(Received 28 November 2000; received in revised form 23 January 2001; accepted 23 January 2001)

Abstract—This study primarily concerns the role of cell wall microstructure in influencing the mechanical behaviour of metallic foams. Three closed-cell foams have been examined, having rather similar relative densities and cell structures but significant differences in cell wall microstructure. It is concluded that these differences can substantially affect the micro-mechanisms of deformation and failure under different types of loading and can also have an influence on the macroscopic mechanical response. Cell wall ductility and toughness are impaired by high volume fractions of coarse eutectic, fine oxide films and large brittle particles, all of which were present in one or more of the foams studied. This impairment can lead to extensive brittle fracture of cell walls, with little energy absorption, even under nominally compressive loading conditions. The influence of cell wall ductility tends to become more significant when the loading state is such that local tensile stresses are generated. © 2001 Acta Materialia Inc. Published by Elsevier Science Ltd. All rights reserved.

Keywords: Microstructure; Foams; Mechanical properties

1. INTRODUCTION

There has been extensive recent interest in the production [1–5] and mechanical properties [6–11] of lightweight metallic foams. There is also interest in layered structures incorporating metallic foams [12, 13]. Some information is now becoming available on the relationships between processing conditions and the size, shape, volume fraction and spatial distribution of the cells within these foams. However, there is still some uncertainty about the role of these factors in determining the mechanical properties.

Several models have been proposed [14–18] for simulation of the mechanical behaviour of metallic foams, based on an idealised representation of the cell structure. However, it is now recognised that most metallic foams show little true periodicity and, as a direct consequence of this, their properties are markedly inferior to those predicted for periodic, defect-free cellular materials. Reductions by factors of up to 50 have been reported [3–7, 19] for some properties. Although it is difficult to quantify the precise significance of the stochastic nature of the cell and cell wall

geometry in terms of its effect on the mechanical performance, some attempts have been made to do so (mostly using finite element modelling [20–23]).

An important point concerning the mechanical behaviour of metallic foams is that the significance of the microstructure of the cell wall material has been largely ignored in most studies, despite the fact that this commonly exhibits features, such as high contents of brittle ceramic constituents, which would have dramatic effects on the performance in corresponding bulk material. In the current work, a systematic study has been made of three different closed cell Al alloy foams, all made by a hydride foaming process. The first material, which is commercially available under the trade-name Alporas, is produced by a melt route, whereas the other two are made using powder metallurgy and sold under the trade-name Alulight. Attention is concentrated both on the cell structures and on the cell wall microstructures, which are significantly different in the three cases.

2. EXPERIMENTAL PROCEDURES

2.1. Material production

The Alporas foam (F1) is produced via a melt route [24], in which calcium (5% wt of the melt mass) is first introduced into molten Al, in order to raise the

[†] To whom all correspondence should be addressed. Fax: 44-01223-334567.

E-mail address: twc10@cam.ac.uk (T.W. Clyne)

viscosity, and TiH_2 (1.6 wt%) is then added. On being introduced into this melt, TiH_2 powder particles decompose to release hydrogen, forming a foamed aluminium product. The other two foams (F2 and F3), based on Al-12Si-0.6Mg and Al-1Mg-0.6Si respectively, were made by a powder metallurgical route [25]. In this process, Al alloy powders are mixed with the foaming agent, TiH_2 (0.4 wt%), and continuously hot extruded into a rod-shaped precursor material. The precursor is then placed into a steel mould and was heated up to temperatures close to the Al alloy melting point. Thermal decomposition of the hydride yields a foamed structure with a dense surface skin.

2.2. Material characterisation

Samples were sectioned by electro-discharge machining (EDM), in order to minimise local cell wall damage. The specimens were infiltrated in vacuum by a low viscosity resin (Epofix, supplied by Struers). The resin was poured onto the sample and, on admitting air to the chamber, was forced into the pores. To ensure good penetration, several pumping-venting cycles were conducted. A blue dye was added to enhance the contrast between the cell walls and the pores. After vacuum impregnation, the specimens were ground with a series of SiC papers and afterwards further polished with 6, 1 and $1/4 \mu\text{m}$ diamond paste. Microstructural examination of polished cross-sections and fracture surfaces was performed using a Jeol-5800 scanning electron microscope, in both secondary and back-scattered modes. Compositional analysis was performed using energy dispersive X-ray spectroscopy (EDS).

All of the foams were characterised in terms of their density, cell morphology and cell wall microstructure. The density was measured by weighing (using a Sartorius balance with a precision of $\pm 10 \mu\text{g}$) of cuboidal specimen, combined with measurement of dimensions using electronic calipers. It was also estimated using image analysis on foam sections. Characterisation of the cell morphology included study of geometrical features, such as the distributions of cell wall thickness and cell size, as well as defects in the cell structure. Images with more than 150 cells were either acquired by an RGB camera or scanned and then analysed using SeeScan and KS 400 image analysis systems.

Cell size data were obtained with the SeeScan system by finding the "diameter" of the pore from the shortest distance between a pair of parallel lines surrounding the pore, so that no part of the pore crossed either line. The cell size was taken as the mean of 36 "diameters", measured at 5° intervals. To measure the cell wall thickness, a KS 400 image analysis system was used. This feature was measured from the line joining the centroids in neighbouring cells. The hardness of the cell wall material was measured using a nanoindenter (Nanotest 100, Micro Materials Ltd.) with load and displacement resolutions of $0.1 \mu\text{N}$ and 0.1 nm . The indenter was a triangular pyramid-shaped

diamond, with the same area to depth ratio as the traditional Vickers pyramid. The hardness was measured using the technique proposed by Oliver and Pharr [26]. The oxide content of the foams was assessed by using a Leco TC-436 microprocessor with an EF-400 electrode furnace. Foam samples with a weight of about 0.2 g were used. The oxygen content was analysed by heating to very high temperature in the presence of excess carbon and measuring the amount of carbon dioxide formed.

2.3. Mechanical testing

2.3.1. Compression tests. Specimens of dimensions $15 \text{ mm} \times 15 \text{ mm} \times 9 \text{ mm}$ were electro-discharge machined from the foamed plates. (Plate thickness for all three materials was 11 mm, and F2 and F3 plates contained dense skins which were removed by electro-discharge machining.) The foam samples were inserted between two stainless steel parallel platens lubricated with anti-friction spray. Uni-axial compression tests were carried out on a servo-hydraulic testing machine equipped with a 10 kN load cell. All tests were conducted under displacement control with a cross-head speed of 0.2 mm min^{-1} . Tests were interrupted and specimens examined after successive increments of $\sim 10\%$ height reduction.

2.3.2. Tensile tests. Tensile specimens were electro-discharge machined from the foam panels. The geometry employed was a rectangular, dog-bone shape. For F1 foam, gauge sections were 8 mm long, 9 mm wide and 11 mm thick, and for the F2 and F3 foams, they were 8 mm long, 8 mm wide and 9 mm thick. In order to prevent crushing in the grip sections, the ends of the foam specimens were vacuum infiltrated by a low viscosity resin. Axial strains were measured via a 11.2 mm gauge length Inston extensometer attached to the reduced section.

2.3.3. Indentation tests. Indentation tests were performed on foam specimens of square section with a side length of 40 mm and thickness of 9 mm. The indenter was 10 mm in diameter and was fixed to the cross-head of a servo-hydraulic testing machine. The displacement rate was set at $20 \mu\text{m s}^{-1}$.

2.3.4. Finite element modeling. Axisymmetric indentation tests have been simulated using ABAQUS/EXPLICIT 5.8 and utilised CAX4R elements (axisymmetric, four-noded, quadratic elements with reduced integration). The finite element model contained 315 elements and the refinement was biased toward the centre of the specimen, where the largest deformations are expected. The bottom nodes of the mesh were fixed. The spherical indenter was modeled as an analytical rigid surface. A contact pair was defined between the indenter and the foam. Contact surface interaction is modeled by specifying a friction coefficient of 0.3. The foamed plasticity model available in Abaqus was used. The elastic properties of the F1 foam were specified by a Poisson ratio, $\nu = 0.33$ and Young's modulus, $E = 1.59 \text{ GPa}$,

the latter having been measured using an ultrasonic resonance technique [27].

3. RESULTS

3.1. Material characterisation

3.1.1. Relative density. The average relative densities of the materials investigated are shown in Table 1. It can be seen that the porosity content was about 86% for the melt route foam and just under 80% for the two powder route foams.

3.1.2. Cell morphology. Typical cell structures, as observed on polished cross-sections, are shown in Fig. 1. It can be seen that all three materials contain heterogeneities and imperfections in their structure. Inhomogeneity was characterised by the width in the cell size and cell wall thickness distributions. These are shown in Table 2. It can be seen that F1 and F3 exhibit both a greater average cell size and a greater spread of sizes than F2. The ratio between the size of the largest and smallest cells was approximately one order of magnitude. The cell wall thickness exhibits essentially the same trend as the cell size, in that F1 and F3 have both a greater average cell wall thickness and a greater spread of thicknesses than F2.

In addition to heterogeneities, morphological defects such as fractured/missing cell walls and cell wall buckling are prominent in the cell structures (Fig. 1). Pores with fractured cell walls form large, non-equiaxed cells with their neighbours. Moreover, these elongated cells often contain buckles in the cell walls. The importance of these morphologically “defective” cells on the deformation behaviour was highlighted by Evans and co-workers [19, 28, 29], using surface strain mapping.

3.1.3. Cell wall microstructure. To improve the contrast between the different phases in the cell walls, back-scattered mode imaging was used (Fig. 2). The cell walls in F1 (Fig. 2(a)) consist of Al dendrites (indicated A) and a network of Al-Ca-Ti eutectic (B and C), with incorporated Al-Ca-Ti-Fe particles (D). The darker areas in the eutectic domain correspond to regions with lower concentrations of titanium (region B). The microstructure is broadly as expected after fairly slow cooling of an Al melt containing Ca and Ti, with relatively coarse dendrites exhibiting pronounced coring.

As illustrated in Fig. 2(b), the cell walls in F2 con-

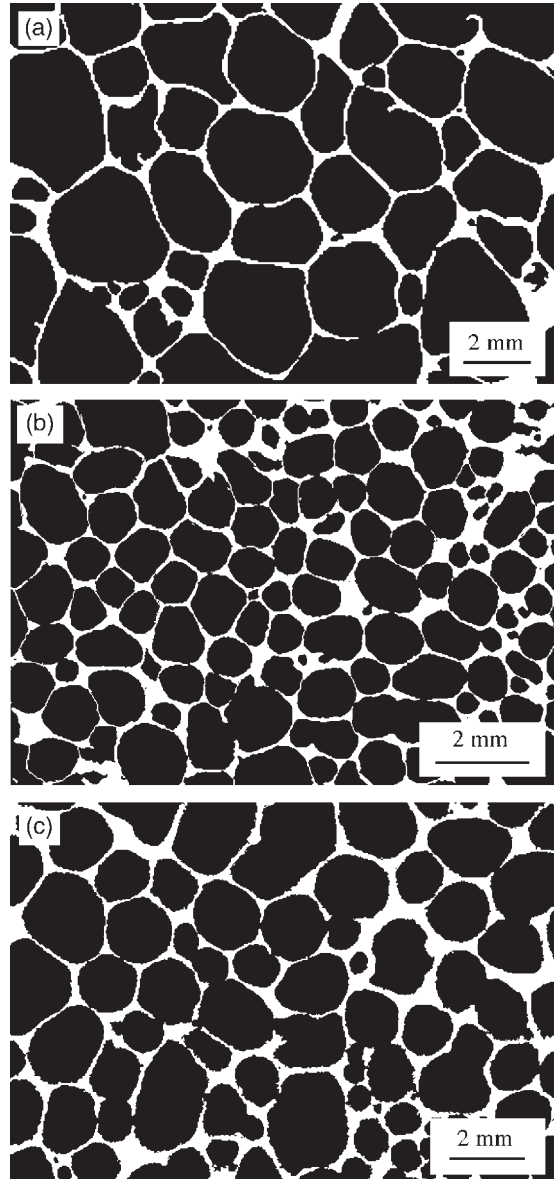


Fig. 1. Binary images showing the cell structure of the materials investigated: (a) F1, (b) F2 and (c) F3.

Table 1. Densities of the three foams (ρ_s is the density of the solid material from which the cell walls are made)

Material	Code	Density ρ (Mg m ⁻³)	Relative density $\rho/\rho_s(-)$
Al foam	F1	0.37	0.14
Al-12Si-0.6Mg foam	F2	0.60	0.23
Al-1Mg-0.6Si foam	F3	0.57	0.21

Table 2. Cell size and cell wall thickness data for the three foams

Material	Code	Cell diameter (mm)		Cell wall thickness (μm)	
		Average	Standard deviation	Average	Standard deviation
Al foam	F1	2.2	0.9	151	49
Al-12Si-0.6Mg foam	F2	1.1	0.4	92	26
Al-1Mg-0.6Si foam	F3	1.3	0.6	141	62

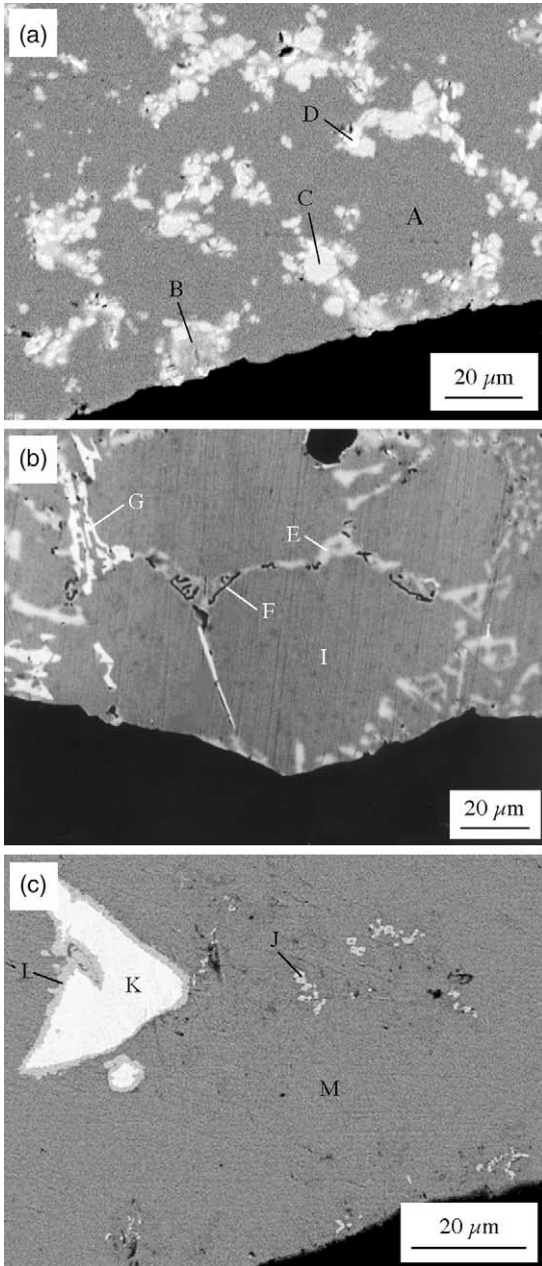


Fig. 2. Backscattered scanning electron micrographs showing the microstructure of (a) F1, (b) F2 and (c) F3.

sist of an interdendritic network of eutectic silicon (E), plus Mg-Si (F) and Mg-Al-Si-Fe (G) phases in a matrix of aluminium solid solution (I). The Mg-Si phase is compositionally consistent with Mg_2Si . The structure is basically the familiar anomalous Al-Si eutectic structure expected of an Al-12%Si alloy, with some primary aluminium dendrites arising from the skewed nature of the coupled zone [30]. This microstructure is expected to give rise to low ductility.

In F3 material (Fig. 2(c)), a Mg-Al-Si-Fe (J) phase was present in the cell walls. Moreover, large Ti-rich particles (K) were randomly distributed within the cell walls. These are presumably residues from the

foaming agent, TiH_2 . The latter were surrounded by a sheath of a Ti-Al phase (L), which is compositionally consistent with $TiAl_3$. This is the expected product when TiH_2 reacts with liquid aluminium to release hydrogen. Such partially-reacted particles were commonly found within cell walls, suggesting that the foaming reaction did not take place very efficiently.

Nano-indentation was performed on polished cross-sections of the cell walls, in order to estimate the hardness of the cell wall material and also to study local variations in hardness, e.g. due to oxide distribution (see next paragraph). A maximum indentation depth of $2\ \mu m$ was set, which was appreciably less than typical cell wall thicknesses. The average values for the aluminium alloy dendrites (H_{Al}) and the multi-phase composite regions (H_{comp}) are listed in Table 3. The hardness values obtained from indentations in the matrix regions showed much less scatter than those from the composite regions.

The foams produced via the powder-based route are expected to contain fine oxide particles within the matrix. The oxide layer, originally present on the surface of the metal powder particles, breaks up during extrusion, leaving a fine dispersion of oxide stringers. Structures of this type have been observed [31, 32] in extruded powder route MMCs, but in general they are too fine to be readily seen by SEM. Oxygen content analysis (Table 3) was carried out in order to explore the probable levels of oxide present in the cell walls. It can be seen from the data in Table 3 that F2 and F3, both produced via a powder route, contained higher oxygen levels than F1, which was produced via a melt route. Since the diameter of the original aluminium powder particles was about $300\ \mu m$, for F2 and $400\ \mu m$ for F3, the oxygen contents shown in Table 3 can be estimated to correspond to prior oxide layer thicknesses of the order of $2\ \mu m$ in both cases. In fact, such thick layers would be a little unusual on Al powder particles and if they were present then some relatively thick, broken up sections might also be expected to be readily visible within the cell walls. This suggests that some further oxidation took place during the foam processing.

3.2. Mechanical behaviour

3.2.1. Compressive response. Typical compressive stress-strain curves for the three materials are shown in Fig. 3. All three curves display a stress maximum, corresponding to the onset of global col-

Table 3. Hardness values for the Al alloy matrix and the multi-phase composite, as measured by nanoindentation of polished cell walls. Also shown are average oxygen contents

Material	H_{Al} (GPa)	H_{comp} (GPa)	O ₂ Content (%)
Al foam (F1)	0.47 ± 0.1	0.58 ± 0.1	0.29 ± 0.001
Al-12Si-0.6Mg foam (F2)	0.94 ± 0.1	1.10 ± 0.3	1.95 ± 0.2
Al-1Mg-0.6Si foam (F3)	0.51 ± 0.1	0.59 ± 0.1	0.94 ± 0.2

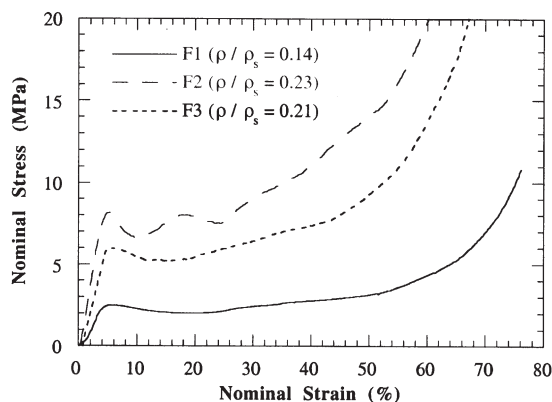


Fig. 3. Compressive stress-strain curves for F1, F2 and F3.

lapse, followed by a load softening region to a “plateau” at which successive bands of cells collapse and densify. Beyond the deformation “plateau”, the stress rises steeply as complete compaction commences. The “plateau” regions exhibits differences among the foams studied. F1 and F3 deform smoothly throughout the entire strain range. However, the plateau stress in F1 is almost constant, in contrast to a slowly increasing stress in F3. In F2, a few minor stress oscillations, which are typically associated with brittle failure, are superimposed upon an increasing stress level.

The specific energy absorbed by the foam up to densification was estimated from the area under the stress-strain curve. Average values are listed in Table 4, expressed per unit volume and per unit mass. The F2 foam absorbs more energy than F1 and F3 foams, although its densification strain is the lowest of the three. This is primarily because relatively high stresses are required for the F2 foam to densify, which in turn is associated both with the porosity content being lower (than that of F1) and the cell wall material being harder and more brittle than either of the other two foams. In practical terms, the energy-absorbing characteristics of the F2 foam may be less attractive than those of the other two, since behaviour in which progressive plastic deformation occurs at relatively low plateau stresses is more likely to ensure uniform and efficient collapse of the material over a range of loading conditions. Such characteristics are also likely to be advantageous when tensile stresses are present (see below).

A consequence of the topology of the cell structures is that strain distributions tend, for all of these

foams, to be locally non-uniform—even at small macroscopic strains. The site of the onset of local plastic deformation depends on the cell structure. Figure 4(a) shows the sequence of deformation events during compression of an F2 sample. At 10% height reduction, deformation is largely concentrated in a plane of cells close to the bottom surface of the sample. The large pore shown in the figure probably triggered this localisation by generating some stress concentration in adjacent areas. (Of course, the presence of the free surface at the plane being viewed will have an effect, but the observed behaviour is still expected to be qualitatively representative of the bulk, at least in terms of these cell collapse characteristics.)

However, deformation was not confined to this region. It can be seen that cells subsequently deformed in shear, spreading outwards from the large pore. As deformation progressed, co-operative collapse occurred, forming both an inclined and an approximately horizontal zone of localised deformation. At 50% strain, the specimen shows some lightly deformed areas, while others are totally crushed. Because some of the cells failed in shear (rather than just concertina collapse of cell walls), the sample exhibits some lateral expansion (“barreling”). Although initiation and growth of the collapse events differed from specimen to specimen, all F2 samples exhibited multiple deformation bands, rather than a single one. During straining, some cell wall fragments were ejected from the boundary cells, indicative of local brittle fracture. This is consistent with the microstructure being primarily composed of coarse Al-Si eutectic, which is expected to have a low ductility.

For F1 and F3 foams, deformation was also spatially inhomogeneous, but it showed a tendency towards progressive collapse, i.e. deformation propagated from an initial site to the rest of the structure. Figure 4(b) shows the development of deformation for an F1 sample. Note that at 50% height reduction, the sample shows almost no lateral expansion. In F1 and F3 foams, structural collapse occurred by plastic buckling of the cell walls and little or no brittle fracture mode was observed. This is expected in view of the higher ductilities associated with the cell wall microstructures of these two foams.

3.2.2. Tension. Typical tensile stress-strain curves for the three materials are presented in Fig. 5. The plots show short regions of plastic flow and strain hardening up to a peak stress. Thereafter, rupture initiates, which is the source of the fall in nominal stress preceding final failure. Once a cell wall fails, stress redistribution occurs, causing the stress to reach the failure level for neighbouring cell walls. This cycle repeated itself until final failure. In most of the specimens, final failure initiated at two sites and generated more than one crack, but only one of them propagated to cause final rupture. Note that the higher cell wall ductility of the F1 foam led to a progressive

Table 4. Specific energy absorption values for F1, F2 and F3

Material	Energy absorbed (MJ m ⁻³)	Energy absorbed (J g ⁻¹)
Al foam (F1)	2.4±0.3	6.5±1.0
Al-12Si-0.6Mg foam (F2)	6.4±1.5	10.7±3.0
Al-1Mg-0.6Si foam (F3)	4.3±1.2	7.5±2.0

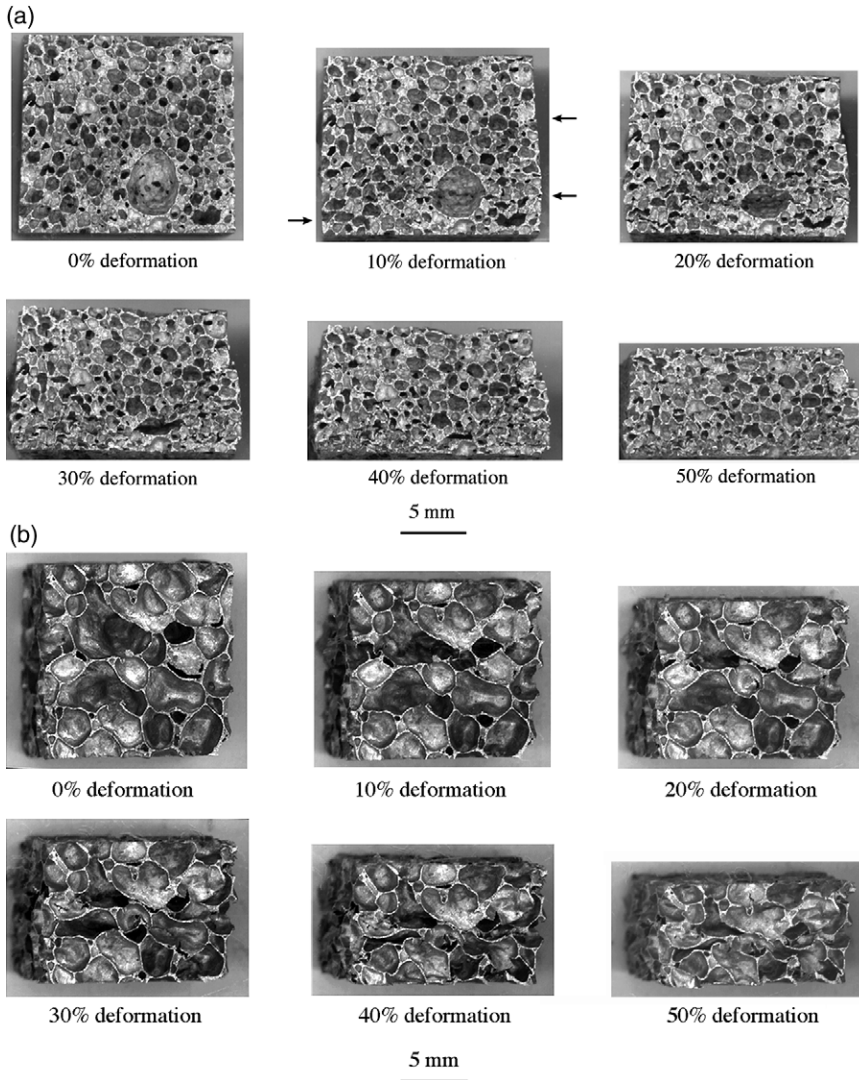


Fig. 4. Evolution of deformation during compressive loading of specimens of (a) F2 and (b) F1.

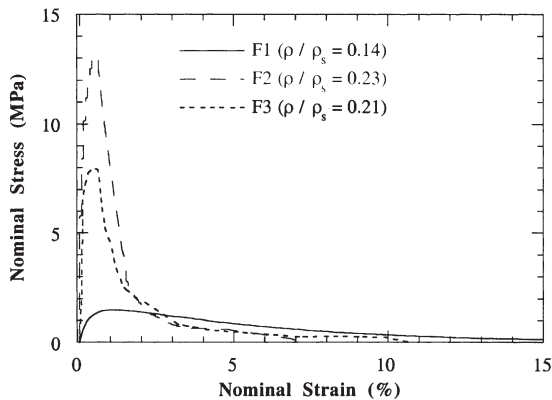


Fig. 5. Tensile stress-strain curves for F1, F2 and F3.

load drop and a nominal failure strain of ~15%, whereas abrupt load drops followed by rupture occurred for F2 and F3 foams. Yield strengths in tension were found to be similar to those in compression—see Table 5. (The compressive yield strength values in this table correspond to the first peak in the stress-strain curve, while the tensile strength was taken as the maximum stress sustained by the specimen.)

Table 5. Yield strengths in tension and compression for F1, F2 and F3

Material	Tensile Strength (MPa)	Compressive Strength (MPa)
Al foam (F1)	1.8±0.4	2.3±0.3
Al-12Si-0.6Mg foam (F2)	9.2±2.2	8.0±2.0
Al-1Mg-0.6Si foam (F3)	6.2±1.3	5.6±1.4

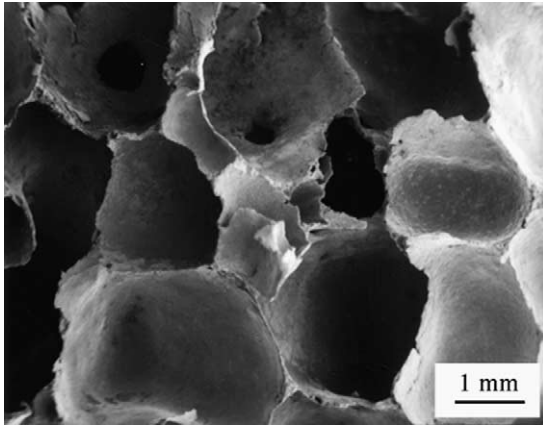


Fig. 6. SEM micrograph of a fracture surface from F1 foam.

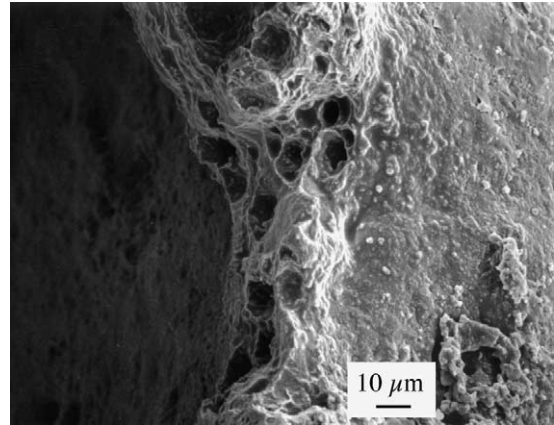


Fig. 9. SEM micrograph of a fractured cell wall in F3. Dimple rupture is evident.

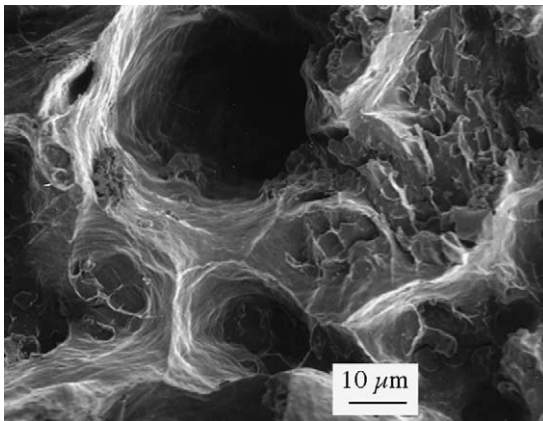


Fig. 7. SEM micrographs of a fractured cell wall in F1. Some evidence of cell wall ductility can be seen.

Post-fracture SEM micrographs are shown in Figs 6–9. The fracture surfaces for all three materials indicate the presence of large cells, which probably acted as stress concentrators and likely sites for failure initiation. Figure 6 shows a typical fracture surface for F1 foam. However, cell wall failure in the three

materials involved different micro-mechanisms. Observation of fractured cell walls at higher magnification (Figs 7–9) reveals that F1 and F3 exhibited quite extensive plastic flow and ductile tearing, whereas F2 failed by a mixture of ductile tearing and brittle fracture. In particular, F1 had sufficient ductility to allow cell wall necking along the crack trajectory (Fig. 7). F2 shows some regions exhibiting ductile failure, as in Fig. 8(a), and areas with a flat, faceted appearance indicative of cleavage cracking (Fig. 8(b)). Also, in Fig. 8(a) a crack meandering across the cell wall is visible. Such cracks—which do not open up significantly and have short lengths (microcracks)—were found to a lesser extent in F1 and F3. In F3, final failure appears to have occurred by ductile void growth and coalescence (Fig. 9). It is likely that such void growth was commonly nucleated at the large Ti-rich particles present in the cell walls (see Fig. 2(c)).

3.2.3. Indentation response. Typical indentation force-displacement curves are shown in Fig. 10. For displacements up to 5 mm (indenter radius), the area of contact between the indenter and the foam

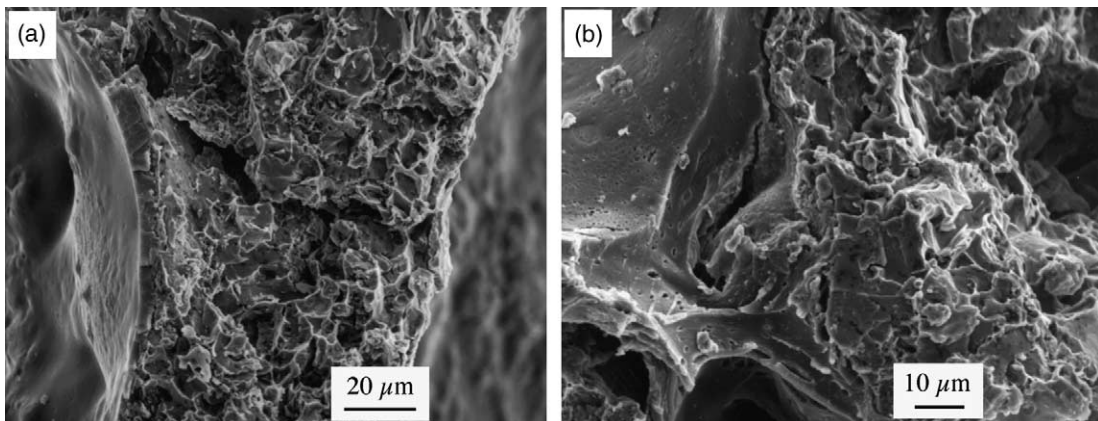


Fig. 8. SEM micrographs of fractured cell walls in F2. Mixed cleavage and ductile tearing features are evident.

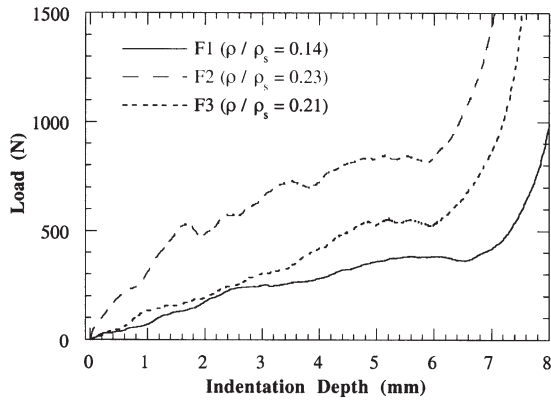


Fig. 10. Indentation force-displacement curves for F1, F2 and F3 materials (indenter diameter=10 mm).

increases continuously, and progressive yielding occurs in a similar manner to that during uniaxial compression. Beyond this point, a plateau is observed. This is associated with quasi-steady state penetration, with cell failure occurring both below the indenter in compression and around the periphery of the indenter in shear. Further displacement results in a rapid increase in the load, as the indenter starts to approach the underlying substrate.

Figure 11 shows torn cell walls at the periphery of the indented F2 foam. Cell wall tearing extends to a distance of about one cell diameter, which is in agreement with previous observations [33]. In F1, however, intact ligaments bridging a torn cell wall were observed (Fig. 12). This suggests that crack extension in F1 occurs by a sequential renucleation of cracks across intervening tough metal ligaments. The contact pressure (plateau load normalised by the indenter contact area) for the F1 foam is a factor of about 2 higher than the uniaxial collapse strength, whereas the ratio

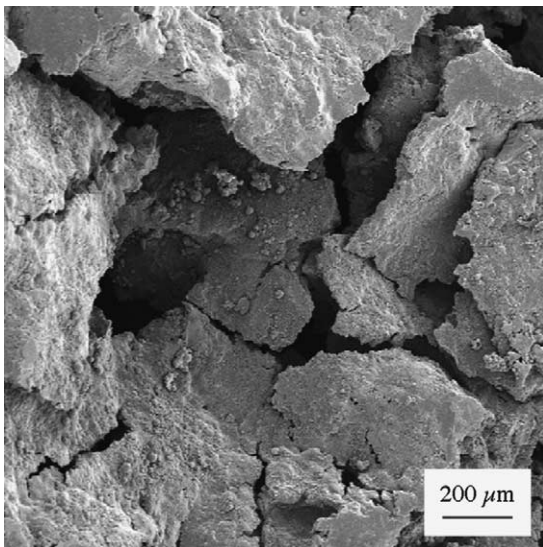


Fig. 11. SEM micrograph showing torn cell walls at the indenter periphery for F2 foam.

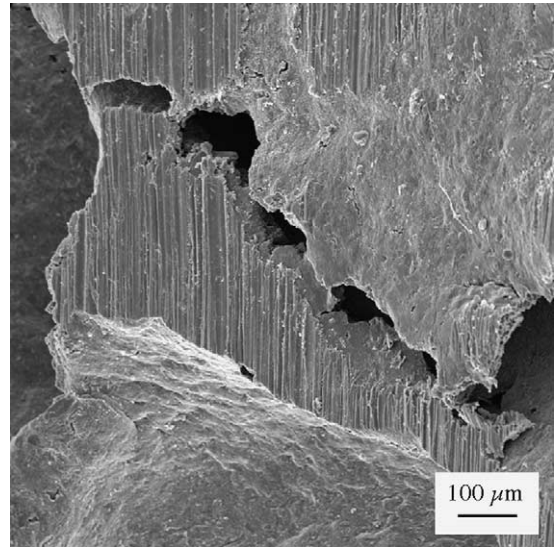


Fig. 12. SEM micrograph showing crack bridging at the periphery of the indented F1 foam.

is only about 1.3 for F2 and F3 foams. Figure 13 shows predicted plastic strain contours (for F1 foam), in the vicinity of a rigid, spherical punch indented to 20% of the foam height. It can be seen that, while material in the vicinity of the indented area experiences large local strains, the surrounding material is essentially undeformed. Since these foams have a plastic Poisson's ratio close to zero [34, 35], the work being done around the periphery of the indenter will predominantly arise from cell wall shearing and tearing, without much compressive radial stress. Such tearing is apparently of greater significance with the relatively ductile cell walls of the F1 foam than with the more brittle cell walls of the other two foams.

4. CONCLUSIONS

The following conclusions can be drawn from this work:

1. Three closed cell metallic foams have been examined. One of these (F1), produced by a melt route, had a high porosity content (~86%) and a cell wall microstructure made up of Al dendrites with some Al-Ca-Ti eutectic and a low oxide content. The other two foams (F2 and F3), which were made by a powder route and thus incorporated higher oxide contents, had somewhat lower porosity contents (~78%). The cell wall microstructure of F2 was essentially that of a coarse (un-modified) Al-Si eutectic, although some primary Al dendrites were also present. The microstructure of F3 was primarily Al solid solution containing Mg and Si, but large Ti-rich particles (residues of the gas-generating agent employed) were also present. The cell sizes were rather similar for the three materials, but those in F2 were somewhat finer and

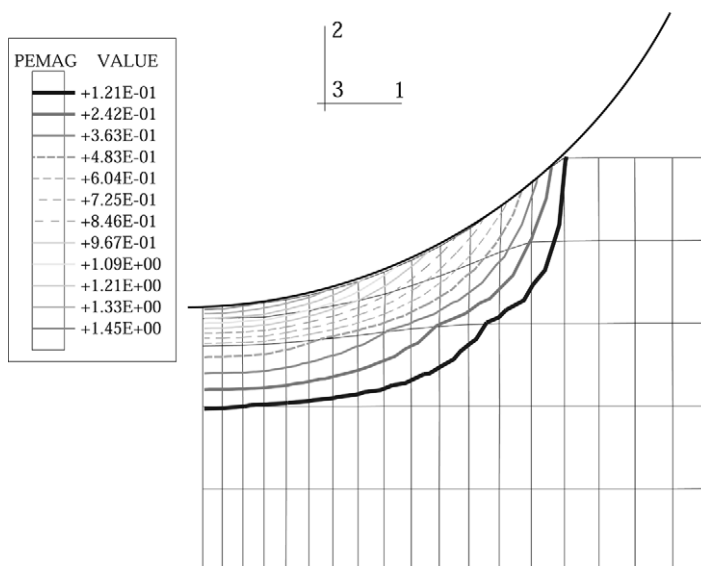


Fig. 13. Deformed FEM mesh, showing predicted plastic strain contours for the F1 foam.

- exhibited less variation than was the case for the other two foams.
- Under compressive loading, all three foams showed inhomogeneous macroscopic deformation, with little change in the lateral dimensions at large strains. Some differences in the deformation pattern were detected between the materials. In F2, once a band of cells had become completely crushed, the band locked up and deformation became localised elsewhere. In F1 and F3, on the other hand, crushing tended to propagate progressively from the initial site of failure throughout the rest of the structure. The mechanisms governing their crushing response were also different. Failure in F1 and F3 occurred by plastic buckling of the cell walls, whereas in F2 brittle fracture of the cell walls was common. This is consistent with the ductility expected on the basis of cell wall microstructures being appreciably lower for F2 than for the other two foams.
 - After tensile loading, study of the fracture surfaces provided insight into the micro-mechanisms of the cell wall failure. F1 showed extensive plastic stretching of the cell walls. This was reflected in the corresponding stress-strain curve, which exhibited appreciable load-carrying capacity over an extended strain range after the onset of plastic instability. F2 failed by a mixture of ductile tearing and cleavage fracture and F3 by ductile void growth. The coarse eutectic structure in the cell walls of F2 is expected to exhibit low toughness. In the case of F3, the cell wall microstructure of Al solid solution is basically expected to be ductile, but the presence of the large Ti-rich particles probably stimulated the void formation which led to failure at relatively low local strains. It is also possible that the presence of fine oxide films in the cell walls promoted more brittle behaviour for the F2 and F3 foams.
 - Indentation tests were carried out to explore the behaviour under localised loading. As the indenter penetrated, there was little or no lateral expansion, so that a circular indent was produced with a diameter close to that of the indenter. The ratio of plastic resistance (plateau load divided by indenter contact area) to uni-axial compressive strength was greater for F1 than for the other two foams. This is thought to be due to the F1 foam exhibiting ductile tearing behaviour under the influence of the shear stresses acting around the periphery of the indenter, whereas for the other two foams the cell walls tended to fracture at weak points, with little extra applied load being required for this to occur.
 - As a general conclusion, it is clear that the nature of the microstructure within the cell walls can have a significant effect on the mechanical behaviour of metallic foams. Optimisation of their performance clearly requires an understanding of the interplay between processing conditions, cell structure, cell wall microstructure and mechanical response characteristics under various types of applied load.
- Acknowledgements*—This work forms part of an initiative concerning metallic foams and associated sandwich and multi-layer structures, which is partially supported by EPSRC. Support for AEM via the State Scholarships Foundation (SSF) of Greece is gratefully acknowledged.

REFERENCES

- Miyoshi, T., Itoh, M., Akiyama, S. and Kitahara, A., in *Porous and Cellular Materials for Structural Applications*,

- ed. D. S. Schwartz, D. S. Shih, A. G. Evans and H. N. G. Wadley. MRS, San Francisco, 1998, p. 133.
2. Ma, L. and Song, Z., *Scripta mater.*, 1998, **39**, 1528.
3. Simone, A. E. and Gibson, L. J., *Acta mater.*, 1998, **46**, 3109.
4. Gergely, V. and Clyne, T. W., *Adv. Eng. Mater.*, 2000, **2**, 175.
5. Gergely, V., Degischer, H. P. and Clyne, T. W., in *Comprehensive Composite Materials, Vol. 3: Metal Matrix Composites*, ed. T. W. Clyne. Elsevier, Amsterdam, 2000, p. 797.
6. Prakash, O., Sang, H. and Embury, J. D., *Mater. Sci. Engng.*, 1995, **A199**, 195.
7. Sugimura, Y., Meyer, J., He, M. Y., Bart-Smith, H., Grenestedt, J. and Evans, A. G., *Acta mater.*, 1997, **45**, 5245.
8. Beals, J. T. and Thompson, M. S., *J. Mater. Sci.*, 1997, **32**, 3595.
9. Sanders, W. and Gibson, L. J., in *Porous and Cellular Materials for Structural Applications*, ed. D. S. Schwartz, D. S. Shih, A. G. Evans and H. N. G. Wadley. MRS, San Francisco, 1998, p. 53.
10. Andrews, E., Sanders, W. and Gibson, L. J., *Mater. Sci. Eng. A*, 1999, **A270**, 113.
11. Fusheng, H. and Zhengang, Z., *J. Mater. Sci.*, 1999, **34**, 291.
12. Markaki, A. E. and Clyne, T. W., in *MetFoam '99*, ed. J. Banhart, M. F. Ashby and N. Fleck. Verlag MIT Publishing, Bremen, 1999, p. 359.
13. Markaki, A. E. and Clyne, T. W., *Mat. Sci. & Tech.*, 2000, **16**, 785.
14. Chen, C. P. and Lakes, R. S., *Cell. Polym.*, 1995, **13**, 186.
15. Warren, W. E. and Kraynik, A. M., *ASME J. Appl. Mech.*, 1997, **64**, 787.
16. Gibson, L. J. and Ashby, M. F., *Cellular Solids*, 2nd ed. Cambridge University Press, 1997.
17. Zhu, H. X., Mills, N. J. and Knott, J. F., *J. Mech. Phys. Solids*, 1997, **45**, 1875.
18. Zhu, H. X., Knott, J. F. and Mills, N. J., *J. Mech. Phys. Solids*, 1997, **45**, 319.
19. Evans, A. G., Hutchinson, J. W. and Ashby, M. F., *Progress Mater. Sci.*, 1999, **43**, 171.
20. Chen, C., Lu, T. J. and Fleck, N. A., *J. Mech. Phys. Solids*, 1999, **47**, 2235.
21. Grenestedt, J. L., *J. Mech. Phys. Solids*, 1998, **46**, 29–50.
22. Grenestedt, J. L. and Tanaka, K., *Scripta mater.*, 1999, **40**, 71.
23. Silva, M. J. and Gibson, L. J., *Int. J. Mech. Sci.*, 1997, **39**, 549.
24. Akiyama, S., Ueno, H., Imagawa, K., Kitahara, A., Nagata, S., Morimoto, K., Nishikawa, T. and Itoh, M., *Foamed Metal and Method of Producing Same*, in *US Patent 4,713,277*, 1987.
25. Simancik, F., Degischer, H.P. and Wörz, H., *Foamed Aluminium-Light Structural and Insulation Material*, in *4th European Conference on Advanced Materials & Processes (Euromat '95)*, (1995). Assoc. Italian. de Metall., Venice/Padua, p. 191.
26. Oliver, W. C. and Pharr, G. M., *J. Mater. Res.*, 1992, **7**, 1564.
27. Chandra, L. and Clyne, T. W., *J. Mater. Sci. Letts.*, 1993, **12**, 191.
28. Bart-Smith, H., Bastawros, A. -F., Mumm, D. R., Evans, A. G., Sypeck, D. J. and Wadley, H. N. G., *Acta mater.*, 1998, **46**, 3583.
29. Bastawros, A. F. and Evans, A. G., in *MetFoam '99*, ed. J. Banhart, M. F. Ashby and N. Fleck. Verlag MIT Publishing, Bremen, 1999, p. 221.
30. Kurz, W. and Fisher, D. J., *Fundamentals of Solidification*, Trans Tech Publications, 1986.
31. Shahani, R. A., *Microstructural Development during Thermomechanical Processing of Aluminium-based Composites*, PhD thesis, University of Cambridge, 1991.
32. Whitehouse, A. F., Shahani, R. A. and Clyne, T. W., *J. Microscopy*, 1995, **178**, 208.
33. Andrews, E. W., Gioux, G., Onck, P. and Gibson, L. J., *Int. J. Mech. Sci.*, 2001, **48**, 701.
34. Shaw, M. C. and Sata, T., *Int. J. Mech. Sci.*, 1966, **8**, 469.
35. Deshpande, V. S. and Fleck, N. A., *J. Mech. Phys. Sol.*, 1999, **48**, 1253.